doi:10.1016/j.jmb.2009.05.066 J. Mol. Biol. (2009) 390, 775–790

JMB

Available online at www.sciencedirect.com

ScienceDirect

ELSEVIER

Multiple Tight Phospholipid-Binding Modes of α-Synuclein Revealed by Solution NMR Spectroscopy

Christina R. Bodner[1,2], Christopher M. Dobson[2] and Ad Bax[1]*

[1]*Laboratory of Chemical Physics, National Institute of Diabetes and Digestive and Kidney Diseases, National Institutes of Health, Bethesda, MD 20892-0520, USA*

[2]*Department of Chemistry, University of Cambridge, Lensfield Road, Cambridge CB2 1EW, UK*

Received 22 April 2009; received in revised form 22 May 2009; accepted 22 May 2009
Available online 27 May 2009

'In dopaminergic neurons, α-synuclein (αS) partitions between a disordered cytosolic state and a lipid-bound state. Binding of αS to membrane phospholipids is implicated in its functional role in synaptic regulation, but also impacts fibril formation associated with Parkinson's disease. We describe here a solution NMR study in which αS is added to small unilamellar vesicles of a composition mimicking synaptic vesicles; the results provide evidence for multiple distinct phospholipid-binding modes of αS. Exchange between the free state and the lipid-bound αS state, and between different bound states is slow on the NMR timescale, being in the range of 1–10 s^{-1}. Partitioning of the binding modes is dependent on lipid/αS stoichiometry, and tight binding with slow-exchange kinetics is observed at stoichiometries as low as 2:1. In all lipid-bound states, a segment of residues starting at the N-terminus of αS adopts an α-helical conformation, while succeeding residues retain the characteristics of a random coil. The 40 C-terminal residues remain dynamically disordered, even at high-lipid concentrations, but can also bind to lipids to an extent that appears to be determined by the fraction of *cis* X-Pro peptide bonds in this region. While lipid-bound αS exhibits dynamic properties that preclude its direct observation by NMR, its exchange with the NMR-visible free form allows for its indirect characterization. Rapid amide–amide nuclear Overhauser enhancement buildup points to a large α-helical conformation, and a distinct increase in fluorescence anisotropy attributed to Tyr39 indicates an ordered environment for this "dark state." Titration of αS with increasing amounts of lipids suggests that the binding mode under high-lipid conditions remains qualitatively similar to that in the low-lipid case. The NMR data appear incompatible with the commonly assumed model where αS lies in an α-helical conformation on the membrane surface and instead suggest that considerable remodeling of the vesicles is induced by αS.

Published by Elsevier Ltd.

Edited by P. Wright

Keywords: α-helix; membrane binding; NOE; Parkinson's disease; SUV

Introduction

α-Synuclein (αS) is a presynaptic protein that is strongly implicated in the pathogenesis of Parkinson's disease. It is found in the form of amyloid fibrils (which are rich in β-sheet structure) in intraneuronal Lewy body lesions characteristic of the disease.[1,2] Three familial mutants of αS have been discovered and correlate with aggressive inherited parkinsonism.[3–5] In presynaptic neurons, wild-type αS is abundant, estimated between 30 and 60 μM.[6] It partitions between a disordered[7] cytosolic form and a vesicle-bound form.[6,8–13] While the details of its function remain largely unknown, αS has been linked to the maintenance of reserve pools of synaptic

*Corresponding author. E-mail address: bax@nih.gov.

Abbreviations used: αS, α-synuclein; NAC, nonamyloid β component; PS, phosphatidylserine; SUV, small unilamellar vesicle; DOPE, 1,2-dioleoyl-*sn*-glycero-3-phosphoethanolamine; DOPS, 1,2-dioleoyl-*sn*-glycero-3-phosphoglycerol; DOPC, 1,2-dioleoyl-*sn*-glycero-3-phosphocholine; HSQC, heteronuclear single quantum coherence; NOE, nuclear Overhauser enhancement; TROSY, transverse relaxation optimized spectroscopy; 3D, three-dimensional; NOESY, NOE spectroscopy; DLS, dynamic light scattering; TEM, transmission electron microscopy; cryo-EM, cryo-electron microscopy; PFG, pulsed field gradient.

0022-2836/$ - see front matter. Published by Elsevier Ltd.

vesicles[14–18] and dopamine homeostasis.[19–21] The protein binds to acidic phospholipids and anionic detergents, and then undergoes a coil-to-helix transition.[6,11,22–27] Seven imperfect 11-mer repeats, containing the consensus sequence KTKEGV, are located in the N-terminal domain of αS and are likely to mediate its lipid-binding properties. The central nonamyloid β component (NAC; comprising residues 61–95) of αS contains a hydrophobic stretch of residues that are at least partially responsible for its high propensity to convert into fibrillar species.[28,29] Long-range interactions between the NAC region and the acidic residues of the C-terminal tail have been identified by paramagnetic relaxation enhancement in NMR studies of lipid/detergent-free samples, and it has been proposed that this interaction stabilizes αS to keep its aggregation propensity in check.[30–32] The 40 C-terminal residues are otherwise reported to lack a defined structure, and solution NMR studies suggest that they are inert to αS–lipid interactions.[26,33,34] Based on chemical shift analysis, the same studies of lipid/detergent-free αS identified a weak α-helical propensity in the N-terminal domain. Later, residual dipolar couplings measurements were used to determine the sodium dodecyl sulfate (SDS) detergent-bound structure of αS, which features two amphipathic α-helices in the N-terminal domain bound to the micelle surface, with the 40-residue C-terminal tail remaining flexible in solution.[35,36]

The structure induced upon phospholipid binding and the exchange dynamics between lipid-free and lipid-bound states are likely to mediate the native state function of αS. However, fibril formation by αS is also affected by lipid interactions and, depending on conditions, membrane mimetics can either enhance or inhibit aggregation kinetics.[37–42] Furthermore, various sources of evidence suggest that the toxicity of αS is due to prefibrillar oligomeric species that are capable of altering membrane permeability, possibly similarly to pore-forming bacterial toxins.[43–47] More recently, it has been suggested that αS is capable of forming transmembrane ion channels in depolarized plasma membranes, and that disease may be triggered by malfunction of a native role in ion conductance.[47–49]

The affinity of αS for phospholipid vesicles of varied chemical compositions has been a topic of intense study pursued by a variety of biophysical techniques (for a review, see Beyer[50]). While a consensus has not fully been reached, the requirements for an acidic headgroup for strong binding and helical transition of αS are observed consistently. The fact that synaptic vesicles contain a high phosphatidylserine (PS) content (up to 12%) has motivated the study of PS-containing synthetic vesicles under a variety of conditions. The additional presence of neutral and zwitterionic lipids, particularly phosphatidylcholine and phosphatidylethanolamine, further enhances binding, perhaps because of the favorable packing properties of these mixed vesicles.[13,22,23,26,51] Electrostatics alone cannot account for the binding properties of αS, as lipid interactions persist, albeit weaker, even with vesicles lacking a net negative charge.[52,53] The degree of saturation and the length of phospholipid chains, which determine the melting temperature and phase transitions of the bilayer, also affect αS binding.[54,55] It has been proposed that αS may preferably bind to regions of lipid disorder or annealing defects and thereby stabilize these types of membrane structure.[18,55,56] In contrast, other studies have identified lipid-ordered domains, such as lipid rafts and 'raft-like' lipids, as being important for the localization of αS to particular regions of the bilayer.[57,58] In all cases, it is clear that αS is finely tuned to its lipid environment, and while charge interactions undoubtedly aid in recruiting αS to the bilayer, specific hydrophobic interactions appear necessary for αS to adopt and sustain a functional structure.

To gain an understanding of αS–lipid interactions on an atomic scale, we have used solution NMR spectroscopy to measure the binding of αS to acidic small unilamellar vesicles (SUVs). Our analysis of NMR intensity and relaxation data led us to propose the presence of competitive αS phospholipid-binding modes that depend on lipid/αS stoichiometry and have been probed over a wide range of relative concentrations (from less than 1:1 to larger than 150:1). We present evidence for the stable oligomeric states of αS bound to lipids, in slow exchange with a free, monomeric, and dynamically disordered aqueous state. Binding of αS to phospholipids is tight, suggesting that the equilibrium in the synapse environment is strongly shifted to the lipid-bound form. Notably, our data are inconsistent with the common "carpet" model, where monomeric αS lies in an α-helical conformation on the membrane surface. On the other hand, our data do not appear to conflict with the experimental EPR observations themselves,[59–62] despite the fact that they have been used to support such a surface-binding model.

Results

Equilibrium partitioning of αS between free state and lipid-bound state

In our characterization of αS–lipid interactions, we have used SUVs (vesicles that are reported to mimic the composition and curvature of synaptic vesicles) consisting of a 1,2-dioleoyl-*sn*-glycero-3-phosphoethanolamine (DOPE)/1,2-dioleoyl-*sn*-glycero-3-phosphoglycerol (DOPS)/1,2-dioleoyl-*sn*-glycero-3-phosphocholine (DOPC) molar ratio of 5:3:2.[63] In agreement with previous reports,[6,11,22,24] we find that αS undergoes a coil-to-helix transition in the presence of these acidic SUVs, as monitored by circular dichroism. Our study has additionally utilized solution NMR spectroscopy to quantify the equilibrium partitioning of αS and to probe its lipid-bound state in a site-specific manner. Peaks observed in the ^{15}N–^{1}H correlation spectrum, which coincide in position with those observed in the

absence of lipids, correspond to residues that retain random-coil behavior; by contrast, residues that experience a different environment when αS binds to lipids will change their chemical shifts and dynamic characteristics. No new or shifted resonance positions are, however, observed upon addition of lipids to αS (Fig. 1a), even though the intensity of many cross-peaks is greatly attenuated upon addition of lipids (Fig. 1b). This result and the absence of any visible broadening of any of the cross-peaks upon addition of lipids indicate that residues that bind to the phospholipids are unobservable in the solution NMR spectrum. Consequently, the decrease in signal intensity in the heteronuclear single quantum coherence (HSQC) spectrum upon addition of lipids reflects quantitatively the fraction of protein molecules for which any given residue has become NMR-invisible by lipid binding. A plot of the observed intensity in the αS spectrum as a function of position in the protein sequence demonstrates that signal attenuation is not uniform across the protein, but that signals from N-terminal residues are attenuated considerably more than signals from residues towards the C-terminus (Fig. 1b). This result importantly demonstrates that: (a) a higher fraction of αS contains immobilized residues near the N-terminus than towards the C-terminus; (b) residues that are not themselves immobilized by lipid binding remain dynamically disordered and random-coil-like, even when other parts of the same protein molecule are immobilized; and (c) multiple distinct and long-lived states of lipid-bound αS must be present. This last point is apparent when noting that contiguous residues of the protein show comparable attenuation, indicative of binding in a concerted manner, but that distinct steps in attenuation profile are observed at certain points in the sequence. This effect is most pronounced between residues 98 and 100, but is also observed between residues 25 and 30; furthermore, at high-lipid concentrations (Fig. 2b), transitions at residues 65, 85, and 120 are also observed. This plateau behavior identifies the presence of distinct bound states of αS, with exchange between them being slow on the NMR timescale ($<10\ s^{-1}$). At low lipid/protein ratios, there exists a pool of protein, where only the first *ca* 25 N-terminal residues are bound and NMR-invisible (referred to as SL1), and a second pool (SL2), where residues 1–97 are invisible. As will be discussed later, strong transferred nuclear Overhauser enhancement (NOE) connectivities for residues 1–100 point to slowly tumbling helical states for SL1 and SL2.

Differences in attenuation are also observed for residues preceding and following Pro120 in the sequence; however, as will be discussed later, the attenuation for the C-terminal residues is of a different origin that is likely to be influenced by the cis–trans equilibrium of Pro117 and/or Pro120 peptide bonds. A similar, less distinct break in attenuation is seen at Pro128, but no transferred NOEs are seen for any of the 40 C-terminal residues, indicating that C-terminal regions with *trans* Pro peptide bonds remain highly dynamic, even in the presence of lipid.

As shown in Fig. 2a, the relative degree of attenuation changes when the protein concentration is lowered, indicating competition between different

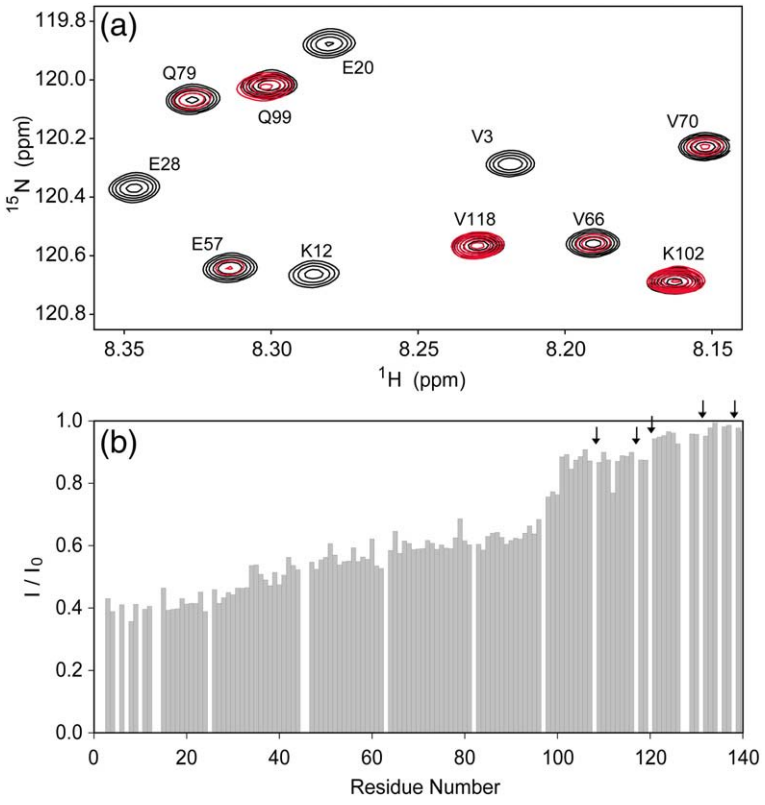

Fig. 1. Effects of the addition of lipid SUVs to the ^{1}H–^{15}N HSQC spectrum of αS, recorded at a ^{1}H frequency of 600 MHz, 293 K, and pH 6.0. (a) A section from the assigned and overlaid HSQC spectra of 150 μM αS in the presence of 0.03% (black) or 0.06% SUV (red). (b) Fractional signal attenuation relative to lipid-free spectra as a function of residue number for 150 μM αS in the presence of 0.03% SUV (wt/vol). The lipid/αS molar ratio is 2.6:1. Missing values correspond to proline residues (arrows), two solvent-exchanged N-terminal residues, and residues whose ^{1}H–^{15}N cross-peaks are significantly overlapped, which have been eliminated from further analysis.

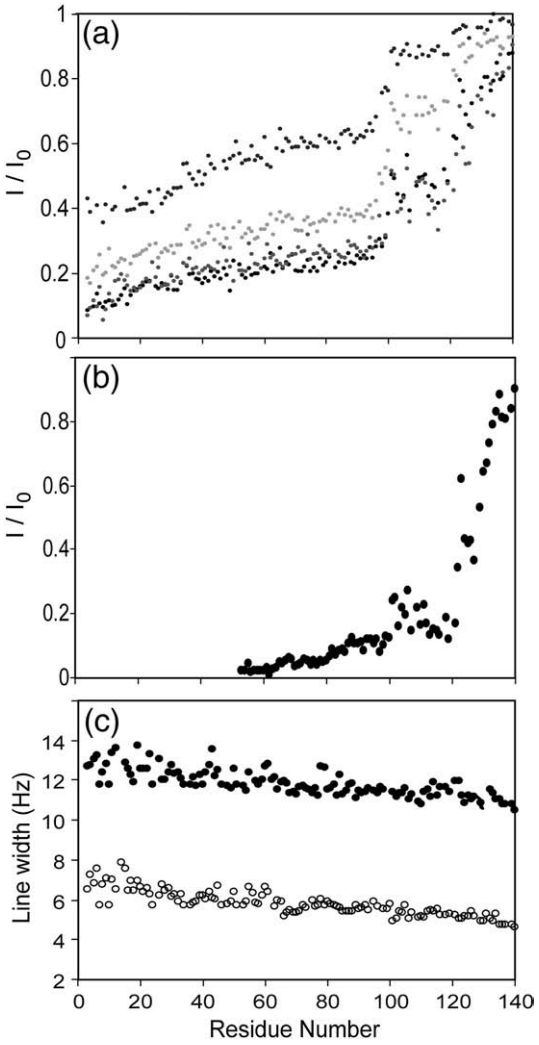

Fig. 2. Impact of αS–lipid binding on ^{1}H–^{15}N HSQC cross-peak intensity and linewidth under lipid-limited and lipid-saturated conditions. (a) In the presence of 0.03% SUV, NMR cross-peak signal attenuation profiles for decreasing concentrations of αS are shown: 150 μM (blue), 75 μM (green), 25 μM (red), and 12.5 μM (black). (b) Attenuation profile for 150 μM αS in the presence of 2.0% SUV, where the lipid/αS ratio is 173:1. Cross-peak intensities of residues preceding V52 were too weak for reliable measurements. Decreased αS concentration or increased lipid availability reduces competition between different binding modes, altering the attenuation profile. Upon lowering of the αS concentration, no significant changes to the profile are observed for lipid/αS ratios >15, where binding appears to be no longer constrained by the lipid-limited condition. (c) ^{1}H (filled circles) and ^{15}N (open circles) linewidths for the same 25 μM αS sample used for the data in (a). Narrow and uniform linewidths show that observed signals correspond to amide groups of residues in the random-coil state.

binding modes. The binding of αS to lipid can be described by equations of the type:

$$\alpha S + \text{Lipid} \underset{K_{d,n}}{\longleftrightarrow} SLn \qquad (1)$$

where, in its simplest form, only two lipid-bound states (SL1 and SL2) are distinguished. The NMR data recorded at high lipid/αS ratio (Fig. 2b), however, suggest that more than two distinct states exist. A highly remarkable and unexpected feature of lipid binding is that the equilibrium of Eq. (1) is in the slow-exchange limit on the NMR timescale, meaning that the lifetime of a molecule in the free state is long compared to T_2*, where the NMR linewidth is given by $(\pi T_2^*)^{-1}$. For αS in the presence of lipids, ^{15}N linewidths ≤5 Hz are observed, indicating that the lifetime of the free state exceeds 100 ms. In addition to exchange between the lipid-free state and the lipid-bound state of αS, exchange between different SL*n* forms may occur; however, considering the absence of visible exchange line broadening, this exchange must again be slow on the NMR timescale.

In order to retain a sufficient population of free NMR-observable αS, we carried out experiments mostly at very dilute lipid concentrations (0.3 mg mL^{-1}) where the SL1 and SL2 binding events are in competition with each other due to limited lipid availability. However, when lowering the αS–lipid ratio in a stepwise manner, we asymptotically reach an attenuation pattern where competition for lipid no longer dominates (Fig. 2a). The differences in attenuation observed as a function of position then provide a direct measure of the SL1- and SL2-bound state populations. For example, under the conditions of Fig. 1 (150 μM αS and 400 μM lipids), attenuation is *ca* 60% for residues 1–25 and *ca* 45% for residues 30–100. This finding corresponds to concentrations of 60% for [SL1 + SL2] and 45% for [SL2] (i.e., *ca* 15% for [SL1]). At lower protein/lipid ratios, the difference in attenuation between residues 1–20 and 30–100 decreases (Fig. 2a), pointing to an increase in the SL2/SL1 ratio.

Our observations are in qualitative agreement with an earlier NMR study that showed residues 108–140 of αS to remain fully observable in the presence of lipid vesicles, while the other residues were observed with a much reduced intensity.[33] The low-intensity signals were interpreted as arising from a minor population of free, disordered αS. However, our results indicate the presence of distinct lipid-bound αS states, which have different sections of their 100 N-terminal residues involved in lipid binding. Distinct boundaries in the C-terminal segment of 40 residues point to distinctly different behaviors for different bound forms of the protein; however, as will be discussed later, we tentatively assign these boundaries to populations of proteins with *cis* X-Pro peptide bonds, with changes in attenuation pattern coinciding with the location of proline residues. Our results differ markedly from the behavior seen when αS binds to SDS micelles. In that case, the first 96 residues adopt primarily an α-helical conformation, and the 40 C-terminal residues retain random-coil characteristics. Moreover, exchange broadening is seen when the SDS/αS molar ratio falls below *ca* 70:1.[36] Differential attenuation of different protein segments upon lipid addition, as observed in our study, cannot be attributed to exchange broadening or variations in the degree

of motional restriction imparted to different residues in the molecule because linewidths are highly uniform and very narrow for all observed resonances (Fig. 2c), and no change in chemical shift is observed for any of the residues upon addition of lipids. As will be shown below, rapid NOE buildup and extensive H^N–H^N spin diffusion in transferred NOE experiments, carried out in the presence of lipids, point to a slowly tumbling, largely helical structure for the "dark state." The absence of significant line broadening for the resonances remaining upon addition of lipids (Fig. 1) then points to a very small generalized-order parameter[64] (i.e., $S^2 < \sim 10^{-2}$) for these observed amide groups.

Estimate of αS–lipid affinity and lipid/αS binding stoichiometry

By fixing the total lipid concentration at 0.3 mg mL^{-1} or ~0.4 mM, we lowered the αS concentration to achieve a ratio where the attenuation profile reaches a plateau (Fig. 2a). This condition is reached at *ca* 25 μM, where 85–90% attenuation is observed for N-terminal αS resonances. The remaining free αS concentration at a total αS concentration of 25 μM is *ca* 3 μM, which drops to *ca* 1.5 μM at the lowest αS concentration probed (12.5 μM). Without requiring knowledge of the number of lipids bound per αS molecule, we can define an apparent total dissociation constant $K_{d,t}$ with respect to the monomer concentration of the lipid:

$$K_{d,t} = \frac{[\alpha S_{free}][Lipid_{free}]}{[\sum SLn]} \quad (2)$$

where $[\sum SLn]$ refers to the total concentration of lipid-bound αS. As we have ensured that we are below the crowding limit, $[Lipid_{free}] \gg [\Sigma SLn]$, so that $[Lipid_{free}]$ is estimated to be in the 0.25–0.4 mM range, yielding a $K_{d,t}$ value in the range of 30–50 μM. Due to morphological changes that can occur in the SUV (as discussed below), we consider all available lipids in deriving the above $K_{d,t}$, including both leaflets of the SUV.

Remarkably, even at very low lipid/αS ratios, a substantial fraction of αS is converted into its "dark state" by lipids; a comparison of samples that contain 75, 150, and 300 μM αS, and each 400 μM (0.03%) lipid (Supplementary Fig. 1) indicates that the absolute concentration of the total lipid-bound αS reaches *ca* 150 μM αS. These conditions represent a ≤3:1 molar stoichiometry of lipid/αS for the bound species. The surface area of a single lipid headgroup situated in a bilayer is only ~0.5 nm^2, which clearly is insufficient to account for the high affinity of αS for lipids in a simple surface-binding mode. A binding mode with such a small area of contact not only appears difficult to reconcile with the immobilization of a large fraction of the αS backbone but also is inconsistent with the slow-exchange kinetics observed for the system. The stoichiometries therefore exclude the possibility that the bound forms simply reflect different states of αS on the surface of the SUV and instead require a drastic rearrangement into a new species containing roughly equimolar fractions of lipid and protein (i.e., dominated by αS by an order of magnitude in mass).

αS immobilization monitored by Tyr fluorescence anisotropy

We also measured fluorescence anisotropy to determine the stoichiometric ratios of lipid/αS binding, and the results are in close agreement with the low lipid/αS ratios determined by NMR titrations. Fluorescence anisotropy increases with the correlation time of the sampled species (up to a maximum value of $r = 2/5$ for samples where the rotational correlation time of chromophore greatly exceeds its fluorescence lifetime) and is therefore an indicator of the degree of immobilization of αS in its bound form. Native αS does not contain any tryptophan residues, and we therefore monitored the fluorescence at the maximum emission wavelength of tyrosine (306 nm) as a function of lipid concentration. Upon lipid binding, fluorescence anisotropy is expected to be dominated by Tyr39 signal, while Tyr125, Tyr133, and Tyr136 will contribute minimally due to their C-terminal position, which remains unperturbed and dynamically disordered at low lipid/αS ratios according to the above NMR data.

Figure 3 shows the rapid increase and near saturation of the fluorescence anisotropy of 500 μM αS as lipid vesicles are added. By the point of addition of 0.1% SUV, where the lipid/αS molar ratio is 2.6, fluorescence anisotropy approaches its asymptotic limit, indicating that the bulk of the change in tyrosine anisotropy signal (attributed to Tyr39) is complete. Under the same sample conditions, the NMR signal intensity data also indicate that more than 60% of Tyr39 residues do not yield a visible back-

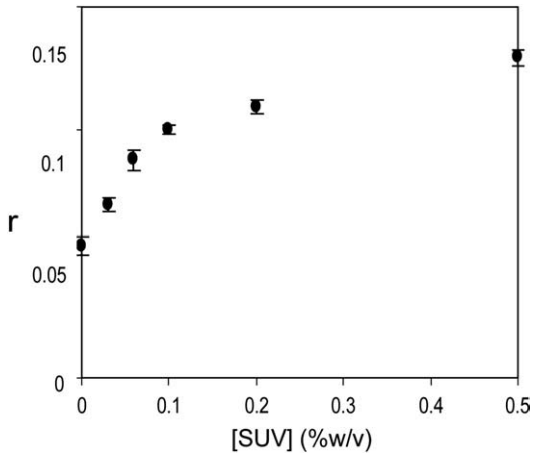

Fig. 3. Fluorescence anisotropy *r* of 500 μM αS as a function of lipid concentration. The emission maximum of tyrosine (306 nm) is monitored. At a lipid concentration of 0.1%, where the lipid/αS ratio is 2.6:1, the change in fluorescence anisotropy nears saturation.

bone amide NMR signal, while the amide signals of the three C-terminal tyrosine remain nearly unattenuated.

Kinetics of binding

As discussed above, the absence of any significant shift or broadening of the observed αS resonances from their random-coil lipid-free positions establishes that the exchange process between the free species and the bound species is slow on the NMR chemical shift timescale. Such slow-exchange rates are not expected for the transient binding and dissociation of monomeric αS on a bilayer surface, but rather argue for the bound form of αS to be separated by a high-energy barrier from the dynamically disordered solution state. Even while no significant broadening of αS resonances is observed upon addition of lipid (Fig. 1a), this does not exclude the possibility of slow-exchange processes between the random-coil state and the immobilized state of the protein. Provided that such processes take place on a timescale that is not much slower than the inverse of the transverse relaxation rate R_2^T of the transverse relaxation optimized spectroscopy (TROSY) component[65] of ^{15}N transverse magnetization, they can be probed conveniently by measurement of these TROSY transverse relaxation rates.[66,67]

In the slow-exchange limit, the observed R_2^T equals the sum of the R_2^T of the highly mobile random-coil state $R_{2\ random\_coil}^T$ and the forward rate of the free-to-bound transition k_{on}. R_2^T values in the lipid-free state for αS are very low (*ca* 2 s^{-1}) (Fig. 4), allowing a straightforward detection of even relatively small contributions resulting from k_{on}. With the exception of several residues for which the intrinsic random-coil hydrogen exchange rate is highest[68] and for which this type of exchange impacts the apparent R_2^T value, transverse relaxation rates in the absence of lipid are quite uniform and very low, in agreement with a highly mobile, disordered, random-coil-like conformation.[31,32,69,70] In the presence of lipids, a significant increase in R_2^T is observed for residues 1–100 (Fig. 4), indicative of k_{on} values in the range 3–5 s^{-1}.

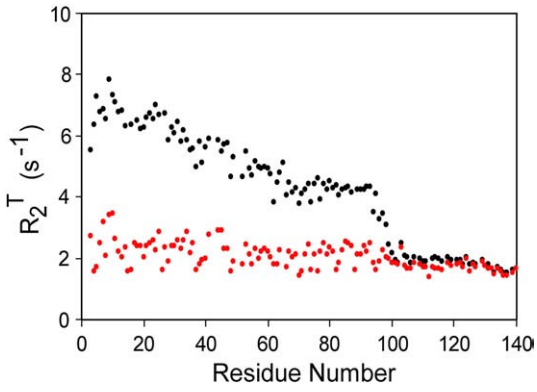

Fig. 4. Transverse relaxation rates of the ^{15}N TROSY component (R_2^T) measured for 600 μM αS in the presence (black) and in the absence (red) of 0.03% SUV at a ^1H frequency of 600 MHz. In the presence of lipids, effective R_2^T is the sum of the intrinsic R_2^T and the forward exchange rate k_{on}. Rates are derived from the monoexponential fitting of intensities recorded in an interleaved manner for 12 transverse decay times: 20, 30, 50, 70, 90, 120, 150, 180, 220, 270, 400, and 500 ms.

The above analysis is oversimplified and, strictly speaking, applies only to cases where the equilibrium involves a single observable state. As discussed above, the case of αS is more complicated because the observed resonance intensity corresponds to the sum of completely free αS and motionally unrestricted segments of different bound forms of αS. For example, for αS engaged in the SL1-type binding mode, residues 25–140 contribute to the random-coil intensities observed in Fig. 1b. One may expect that αS molecules whose 20–24 N-terminal residues have been immobilized by binding have shorter T_2^T values for observable residues that immediately follow this bound segment, thereby giving rise to an increase in the apparent R_2^T even if $k_{on} \approx 0$. The absence of significant multiexponentiality for the transverse magnetization decay curves for these residues suggests the presence of rather sharp transitions between ordered and disordered residues, as observed previously for amyloid fibrils.[71]

A second complication that arises in the analysis of R_2^T data relates to the possibility of exchange between different bound forms. For example, the NMR-observable resonances for the 25–100 region of SL1 will become NMR-invisible upon SL1 → SL2 transition, which may occur at its own specific rate. Therefore, each TROSY transverse relaxation process could occur with different R_2^T values for the different components that contribute to a given random-coil resonance position. In practice, decay curves are reasonably close to monoexponential (Supplementary Fig. 2), indicating that transitions between different bound forms, if present, do not occur on a timescale that is much faster than the random-coil-to-lipid-bound transitions.

A second procedure that is used to evaluate the timescale of the exchange process is based on saturation transfer NMR experiments. With selective saturation of the magnetization of phospholipid methylene resonances at 1.16 ppm, magnetization transfer to αS amide protons manifests itself in an attenuation of a subsequently recorded HSQC spectrum (Fig. 5). Experiments were carried out in the same manner as used previously to monitor magnetization exchange between aliphatic resonances of the detergent SDS and αS molecules that are 100% partitioned on the SDS micelle surface.[35] The experiments were carried out in a difference mode, permitting quantitative measurements of the fractional attenuation of various resonances in the αS spectrum to be made. The experiments show a relatively uniform (*ca* 2%) attenuation for the NAC region of the αS backbone (residues 65–96). Although an increase in NOE effect is evident towards the N-terminus, its magnitude is roughly propor-

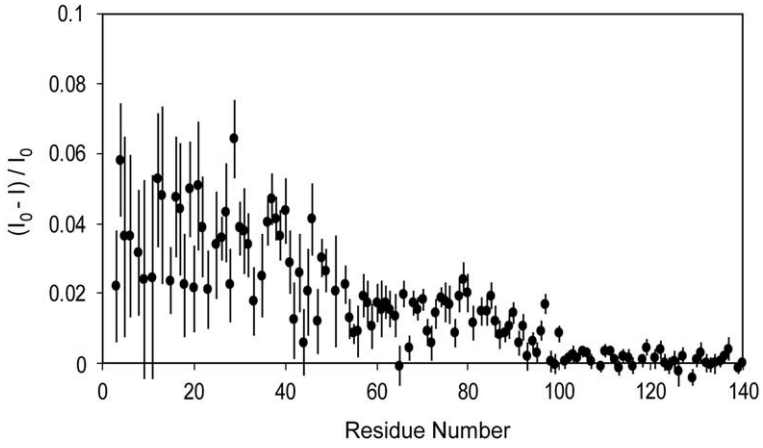

Fig. 5. Lipid-to-αS NOE magnetization transfer as monitored by fractional attenuation of ^{1}H–^{15}N HSQC intensities when the HSQC spectrum is preceded by selective saturation of phospholipid methylene resonance at 1.16 ppm. The sample contains 150 μM perdeuterated αS and 0.03% SUV. The spectra with and without lipid saturation are recorded in an interleaved mode, applying a 1.5-s presaturation with a 21-Hz radiofrequency field strength at either 1.16 or −10.0 ppm.[35] The strongest NOE transfer is observed for N-terminal residues that also exhibit the highest signal attenuation, indicative of the highest partitioning into the "dark state." Error bars correspond to the estimated uncertainty calculated from the signal-to-noise ratio of each correlation.

tional to the fractional attenuation in the reference spectrum (i.e., it reflects the population of each residue in the lipid-bound "dark state"). The fact that magnetization can be transferred from the "dark" lipid-bound state to the isotropic free state is consistent with a transition from bound to free αS on a timescale that is comparable to the longitudinal relaxation rate of αS amide protons (~1 s). Although the scatter in the attenuation profile increases towards the N-terminus, this effect is largely a consequence of the lower signal-to-noise ratio observed for the N-terminal residues as a result of their lower intensities in the presence of lipid (Figs. 1 and 2); indeed, the attenuation due to NOE transfer from the lipid resonances appears quite uniform and gradual. However, as will be discussed below, this observation does not exclude differential contacts between protein residues and lipid molecules: $^{1}H^{N}$–$^{1}H^{N}$ NOE equilibration in the dark state is shown to be rapid and will therefore largely smoothen out any such differential lipid–amide NOE transfer.

"Dark state" of αS probed by transferred NOE

Lipid-bound residues of αS are likely to tumble at a rate that is determined simply by the Brownian diffusion of the "dark-state" particle; this diffusion has been shown to be slow and therefore will cause a very rapid transverse relaxation of nuclear spin magnetization, precluding its contribution to signals in HSQC or TROSY-HSQC NMR spectra. However, slow exchange of molecules between the immobilized state and the random-coil state of the protein allows the characteristics of the NMR-invisible "dark state" to be probed indirectly via ^{1}H–^{1}H NOE correlations, effectively similar to the well-known transferred NOE experiment.[72,73] We therefore recorded two sets of three-dimensional (3D) NOE spectroscopy (NOESY) spectra in the presence of 0.06% lipid. One experiment, HMQC-NOE-HMQC,[74,75] labels in the F_1 dimension the ^{15}N frequency of the amide from which proton magnetization originates prior to NOE mixing, and then reads out the $^{15}N(F_2)$ and $^{1}H(F_3)$ frequencies of the observed amide group. In another complementary 3D NOESY-HMQC experiment,[76] the frequency of the originating amide proton is mapped on the F_1 dimension of the NMR spectrum, with the F_2 and F_3 dimensions again revealing the frequencies of the spins involved. This complementary set of 3D NOESY spectra allows the identification of both ^{1}H and ^{15}N frequencies for each of the two amides associated with any given NOE cross-peak, thereby resolving any ambiguities arising from extensive spectral degeneracy in any individual ^{1}H or ^{15}N dimension. The experiment utilized only amide-selective pulses of the EBURP and REBURP varieties,[77] allowing the experiment to be repeated relatively rapidly[78] and thereby affording high spectral resolution in each of the indirect dimensions.

For spins that are located on a protein initially in the random-coil state but exchange with the dark state and back again during the NOE mixing time, the transfer of magnetization from each amide proton to its proximate spins, which takes place during the time that the backbone is immobilized, will be observed as NOE cross-peaks. Indeed, the 3D NOE spectra (Fig. 6) show large numbers of i to $i \pm n$ NOE cross-peaks (up to $n = 6$) for this perdeuterated protein, despite a relatively short (100 ms) NOE mixing time. A control experiment, recorded in the absence of lipids, shows virtually no NOE intensity other than very weak sequential ($n = 1$) connectivities (data not shown), confirming that NOE buildup has taken place in the dark state. The majority of the observed signal (*ca* 75%) in fact corresponds to spins that have never exchanged with the dark state during the NOE mixing time, and these spins give rise to intense diagonal resonances. Sequential cross-peaks between adjacent amides, however, correspond to spins that have switched to the immobilized state and back during the NOE mixing period, as a result of physical exchange of protein molecules from the free state to the "dark state" and back. While immobilized, NOE transfer of magnetization is fast, giving rise to extensive spin diffusion; there-

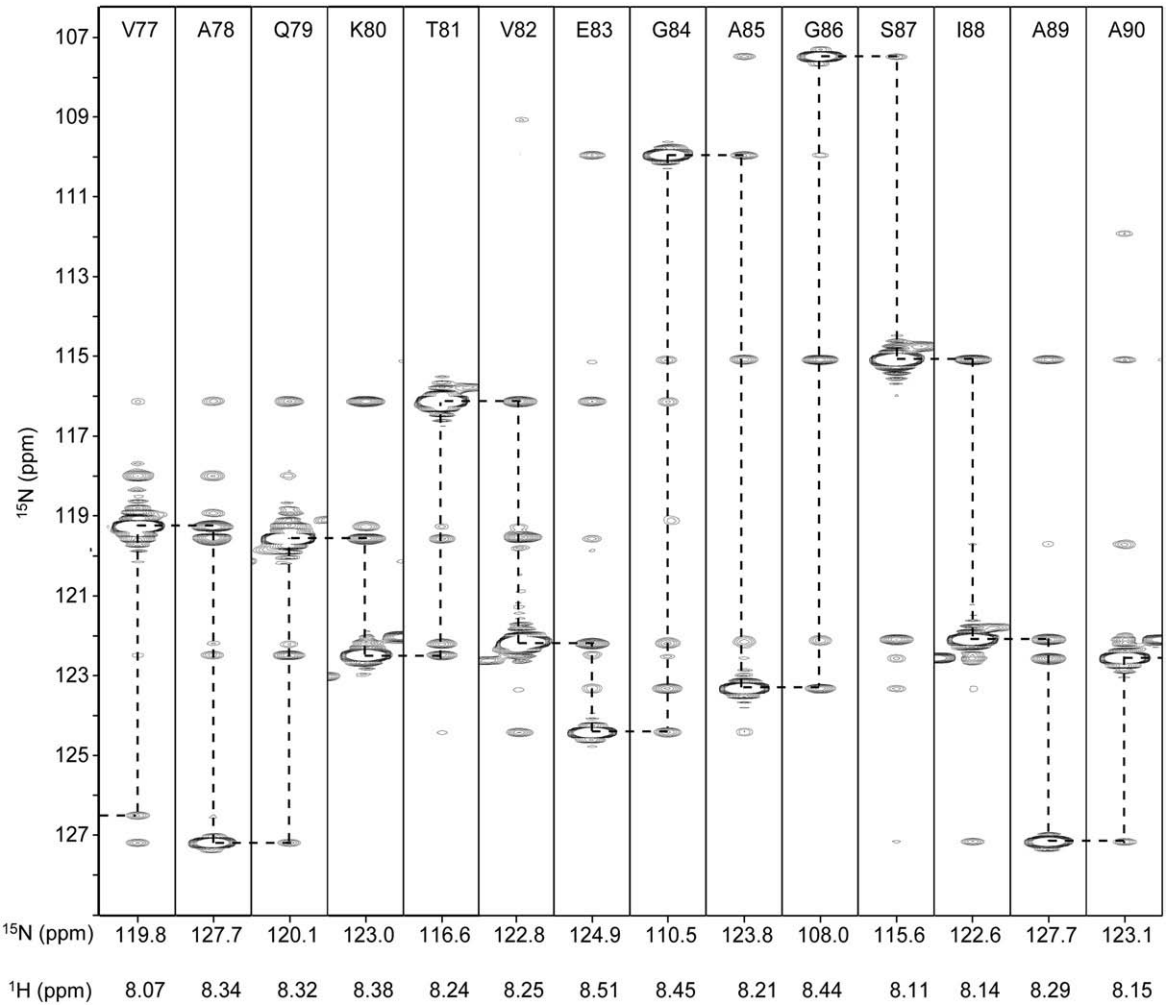

Fig. 6. Series of strip plots for residues 77–90, taken orthogonal to the ^{1}H frequency axis of a 600-MHz 3D HMQC-NOESY-HMQC spectrum labeled with ^{15}N frequencies in both F_1 and F_2 dimensions, recorded for 600 μM αS in the presence of 0.03% SUV and using a 100-ms NOE mixing time. The use of two ^{15}N dimensions in this experiment capitalizes on the greater dispersion of ^{15}N frequencies relative to ^{1}H frequencies to resolve ambiguities in the poorly dispersed spectrum of αS. Spin diffusion undergone by αS in the helical bound state manifests itself in the extensive i to $i\pm n$ amide cross-peaks.

fore, for molecules that contribute to (i, $i\pm1$) cross-peaks, diffusion of magnetization from i to $i\pm2$, $i\pm3$, and even further is also observed. Indeed, for the vast majority of amides in the SL1 and SL2 regions, H^N–H^N connectivities to eight or more amide protons adjacent to each other can be detected at contour levels somewhat lower than those shown in Fig. 6. The rapid spin diffusion along the peptide chain, together with the universal decrease in i to $i\pm n$ H^N–H^N cross-peak intensity with increasing n, indicates that sequential distances ($|n|=1$) are shorter than medium-range or long-range H^N–H^N distances ($|n|\geq2$), strongly pointing to a largely helical conformation for the dark state, in agreement with α-helical circular dichroism results. The absence of any long-range NOEs ($n>8$) is consistent with such an α-helical conformation.

A second simple experiment that is used to probe NOE magnetization transfer in the dark state selectively inverts ^{1}H magnetization of individual types of methyl groups. The data shown in Fig. 7 illustrate this experiment for Leu-$C^{\delta1}H_3$. Transfer of magnetization to nearby amides after an NOE mixing period can then be measured by recording the difference between spectra with methyl group inversion and spectra without methyl group inversion. For this purpose, a perdeuterated αS sample with specific methyl protonation of Ile, Val, and Leu was prepared[79] and again examined in a sample containing 0.06% lipid. In the ^{13}C spectrum, the Leu-$C^{\delta1}$ (24.5 ppm) nuclei resonate sufficiently downfield (>4 ppm) from Val $C^{\gamma1}$, Val $C^{\gamma2}$, and Ile C^{δ}, such that their attached protons can be inverted selectively by a bilinear pulse,[80,81] while also partly inverting the Leu-$C^{\delta2}H_3$ proton spins at 23.1 ppm. αS contains four Leu residues at positions 8, 38, 100, and 113 in the sequence, and the Leu-$C^{\delta1}H_3 \rightarrow H^N$ NOE spectrum (Fig. 7a) shows cross-peaks only to the intra-residue amides and sequentially adjacent amide groups. This NOE transfer must arise from the corresponding Leu-$C^{\delta1}H_3$ group while in the dark state, and the NOE difference effect is large for Leu8

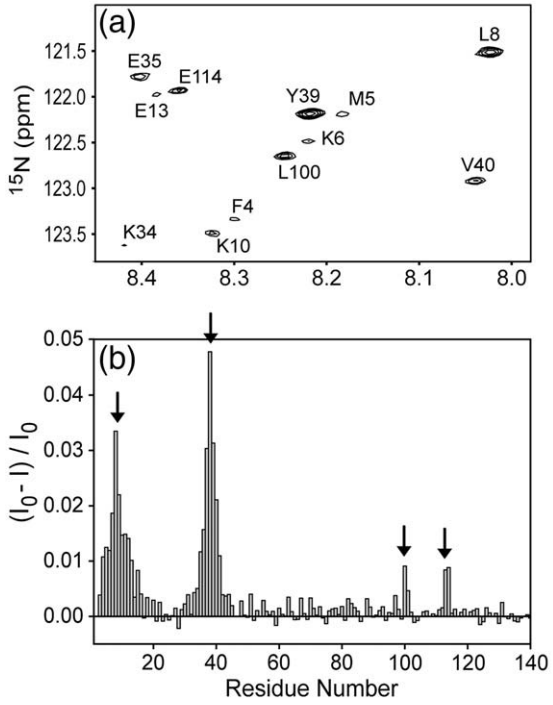

Fig. 7. NOE effect from Leu-$C^{\delta 1}H_3$ methyl groups to backbone amide protons, as monitored by the intensity of ^{15}N–^{1}H HSQC correlations for a sample of 600 μM (I, L, V) αS in the presence of 0.06% SUV, when the ^{15}N–^{1}H HSQC spectrum is preceded by selective inversion or noninversion of Leu-$C^{\delta 1}$ methyl protons (see Materials and Methods) using a 250-ms NOE mixing period. The protein is uniformly enriched in ^{15}N and ^{2}H, with selectively labeled $^{13}C^{1}H_3$ groups for Ile, Leu, and Val. (a) Section of the difference HSQC spectrum showing the differential intensities of leucine and their sequentially adjacent residues. (b) Corresponding histogram plotting the fractional change in signal intensity as a function of protein sequence; positions of leucine residues are marked by arrows.

and Leu38 and extends over a significant number of residues (Fig. 7b). In contrast, only weak intraresidue and (i, i+1) cross-peaks are observed for the dynamically disordered residues Leu100 and Leu113 in the two-dimensional NOE difference spectrum (Fig. 7).

Size of the αS–lipid oligomeric particle

Dynamic light scattering (DLS), transmission electron microscopy (TEM), and cryo-electron microscopy (cryo-EM) confirm the lipid SUVs in the absence of αS to be nearly spherical unilamellar vesicles of *ca* 25 nm diameter (Fig. 8a). However, addition of αS at the relatively high protein/lipid ratios used in our NMR experiments seriously disrupts these SUVs and results in a rearrangement that forms much larger structures, including multilamellar vesicles, branched vesicles, and tubular structures (Fig. 8b–d). DLS is strongly weighted towards the presence of large particles and, under all conditions studied, reveals the presence of a small fraction of very large aggregates (>5 μm), prohibiting characterization of the size distribution of smaller particles in the solution. Both TEM and cryo-EM also indicate the formation of large structures. TEM measurements were, however, carried out following dehydration with the substrate adhering to a lipophilic thin carbon coating; this procedure may therefore affect the structures formed and observed by TEM. Similarly, sample blotting prior to cryo-EM flash freezing has an unknown effect on the protein/lipid ratio, and adhesion to the lacey carbon mesh of the grid may impact the morphology of protein–lipid aggregates, making it difficult to evaluate to what extent the images (Fig. 8) reflect the distribution of particles in solution.

In order to characterize the size of the "dark-state" particles under the conditions of our NMR sample solutions, we therefore have also investigated the particles by translational diffusion rates as measured by NMR pulsed field gradient (PFG) techniques.[82] The diffusion rates of both the protein and the lipid SUVs were measured as isolated species, as well as in mixed samples. Because the ^{1}H signals of fatty acid lipid signals overlap with those of aliphatic αS signals, measurements were carried out on perdeuterated αS, using its amide signals as markers for the protein diffusion rate and the terminal alkane methyl signals for the diffusion of the lipids. When observing amide ^{1}H signals in a PFG diffusion experiment, care needs to be taken to avoid interference between the diffusion rate of water and the diffusion rate of protein molecules,

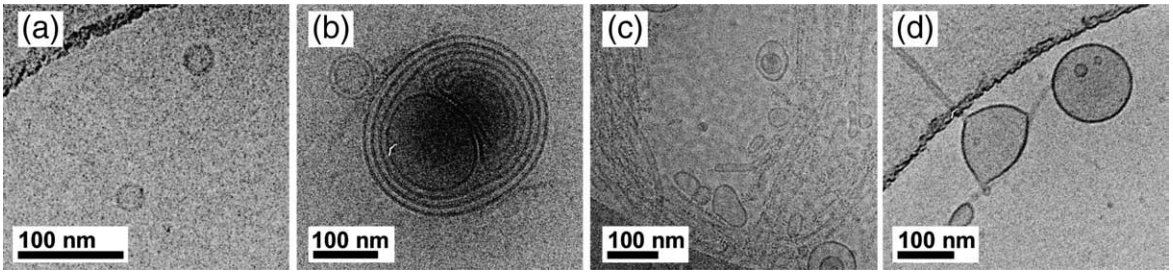

Fig. 8. Cryo-EM images for a sample of 0.03% DOPE/DOPS/DOPC SUVs in the absence (a) and in the presence (b–d) of 600 μM αS. In the absence of αS, vesicles are relatively uniform (20–40 nm in diameter). Destabilization of the vesicle by αS interaction results in gross rearrangements, with the formation of large, multilamellar (b); tubular (c); and pinched, branched, and tubular structures (d). The dark ridges on the top left of (a) and (d) and on the bottom left of (c) correspond to the boundaries of the carbon support of the grid.

as amide protons can exchange with water during the relatively long mixing period of the diffusion experiment. In order to minimize this effect, we carried out measurements at 10 °C and pH 6, where the intrinsic hydrogen exchange rates for most amide protons can be calculated and fall well below 1 s^{-1}.[68] The impact of hydrogen exchange on the measured diffusion decay curve can also be reduced by using the shortest possible diffusion delay, during which hydrogen exchange between solvent and protein takes place; however, this limits the measurement for slowly diffusing large particles, where both longer diffusion delays and strong gradients are required. Instead, we therefore mitigate the impact of hydrogen exchange on PFG diffusion measurements by starting the measurements at gradient strengths G_o, where the rapid initial intensity decay caused by the diffusion of free water is mostly complete (compare Fig. 9 and Supplementary Fig. 5).

Experimental measurements of the hydrogen exchange rates for free αS are generally in good agreement with the values predicted for unstructured peptides[68] (Supplementary Material), as expected for this intrinsically unstructured protein. In the presence of lipids, however, the apparent hydrogen exchange rate measured from the effect of water presaturation on the intensity attenuation of amide signals[35] becomes much greater (Supplementary Material). This can be attributed to a rapid exchange of protons of the serine and threonine hydroxyl groups with solvent, which then causes a rapid equilibration of their nuclear spin magnetization with backbone amide protons through homonuclear NOE effects in the slowly tumbling "dark state." Consequently, amide signal decay in the PFG diffusion experiment of lipid-containing αS samples is governed by a combination of the diffusion rates of water, free αS, and lipid-bound αS. With a PFG mixing time (500 ms) that is considerably longer than the inverse of the free-to-lipid-bound αS conversion rate (*ca* 200 ms), the tail of the PFG decay curve at high gradient strengths is governed by the average of lipid-free and lipid-bound αS, weighted by the relative amide intensity observed for these two states. Under low-lipid conditions (see Fig. 9), analysis of the intensity attenuation pattern indicates that 68% of the total integrated amide ^1H intensity corresponds to lipid-free αS. With the diffusion rate of free αS known from a separate measurement, this results in a diffusion rate of 4.1×10^{-11} m^2 s^{-1} for lipid-bound αS (Table 1). While this diffusion rate is only 30% slower than that for free αS, it corresponds to a radius of hydration R_h of 37±2 Å or to a total mass of *ca* 150 kDa if the lipid-bound state is assumed to be relatively compact. Under the high-lipid conditions of Fig. 9, where effectively all of the αS is lipid-bound, the signal decay as a function of gradient strength is observed to be highly nonexponential, even at gradient strengths where all the ^1H_2O signals have decayed; decay becomes much slower than even that observed for isolated SUVs (Fig. 9), pointing to particle sizes much larger than those of the SUVs. The highly nonexponential decay of the lipid-bound αS indicates the presence of a wide distribution of particle sizes, ranging from smaller than 25-nm SUVs to much larger aggregates (*ca* 150 nm), consistent with cryo-EM observations (Fig. 8).

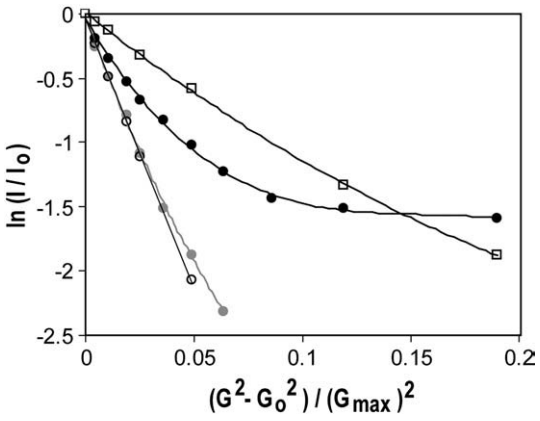

Fig. 9. PFG diffusion plots for αS and SUVs in isolation and in mixed samples. αS (150 μM) in the absence of lipid (open circles) and in the presence of 0.03% (gray circles) or 2.0% (black circles) lipid. Two percent DOPE/DOPS/DOPC SUV in the absence (open squares) of αS. The plot for free αS shows a linear correlation, while all other series show differing degrees of nonlinearity attributable to the heterogeneity of the species being measured. Diffusion delays of 500 ms were used; for αS, the signal decay of the entire amide envelope region is used for intensity measurement. For the sample 150 μM αS/0.03% SUV, 68% of the observed total intensity corresponds to lipid-free protein (note that for lipid-bound protein, only about half of the residues yield an observable intensity). Plotted is the natural logarithm of the ratio between the observed total amide proton intensity I and the value I_o measured at 6% of the maximum gradient strength (87 G cm^{-1}) (i.e., G_o=5.2 G cm^{-1}). In order to avoid contamination from direct solvent exchange with amide protons, we recorded data at pH 6.0 and 10 °C.

Table 1. Translational diffusion rates measured by PFG NMR

Sample	D_s ($\times10^{-11}$ m^2 s^{-1})	R_h (Å)[a]
150 μM αS[b]	5.77±0.12	26.6±0.5
150 μM αS[b] + 0.03% SUV	4.1±0.2	37±2
150 μM αS[b] + 2.0% SUV	0.15±0.01	990±30
2.0% SUV[c]	0.99±.03	152±5

All samples were contained in a 13-mm Shigemi microcell containing 94% H_2O/6% D_2O. Measurements were carried out at pH 6.0 and 10 °C.

[a] Radius of hydration R_h, assuming that the particle is spherical. Under these conditions, the R_h for a standard sample of HEW lysozyme was measured to be 19.5±0.4 Å.

[b] Measured for the envelope of αS amide proton signals.

[c] Measured for the lipid methylene signal at 1.16 ppm in a sample lacking αS.

Discussion

The ability of solution-state NMR to measure processes taking place over a wide range of timescales has made it a powerful tool for probing the dynamics

of αS in the presence of lipid vesicles. Although the long correlation time of lipid-bound αS precludes a direct NMR observation of the lipid-bound state of αS, the phenomenon of slow exchange between bound αS and its disordered free state provides a convenient condition for spying on the 'invisible' lipid-bound state, which is of particular interest in the present study. The slow-exchange kinetics results in the observation of narrow lines for the disordered state and allows us to capitalize on conventional NMR techniques to probe the structural and kinetic details of the αS–lipid complex. Thus, transverse relaxation measurements of the backbone ^{15}N nuclei have been utilized to determine the rates at which αS exchanges from a disordered random-coil state to the lipid-containing "dark state." In addition, NOE transfer experiments have provided information on the contacts made between protein backbone and lipid moieties, and also reveal the dynamic characteristics of the bound state.

In stark contrast to detergent micelles studied previously, a marked loss of NMR signal intensity in the ^{1}H–^{15}N HSQC spectrum of αS is observed upon addition of lipid vesicles; residual intensity varies in a stepwise manner along the αS sequence, without significant concomitant line broadening of attenuated resonances. This observation unequivocally establishes the presence of long-lived lipid-associated "dark" states that are characterized by long rotational correlation times. Although, at least in principle, the formation of the "dark state" could be lipid-free (i.e., lipids could act as catalysts for the formation of annular or tubular pore-like oligomeric structures previously observed in the absence of lipids),[45] magnetization transfer between lipid and protein resonances (Fig. 5) argues strongly against the presence of lipid-free aggregates in our samples.

The attenuation profile of amide proton NMR signals, which shows a series of more or less distinct plateaus when plotted as a function of position in the protein sequence (Figs. 1 and 2), provides evidence for a number of distinct lipid-bound species. As has been shown for flexible regions flanking structured regions of molten globule[83] or amyloid fibril cores,[71] the transition between immobilized and flexible domains can be quite sharp, spanning just a few residues. Moreover, αS increasingly partitions into the NMR-unobservable membrane-bound state with increasing lipid concentration; indeed, even at the lowest concentrations (lipid/αS molar ratio ≈1), *nearly* 50% of the protein population has its N-terminal region (residues 3–25) sequestered into the lipoprotein complex. Assuming that all lipids are sequestered, this near-50% attenuation of signals of the N-terminal amide protons of αS in the presence of a near-equimolar concentration of phospholipids points to a lipid/αS stoichiometry of as low as 2:1 for the lipid-bound state.

At lipid/αS molar ratios above ~15, the resonance intensities of the 40 C-terminal amide groups are also substantially attenuated, indicating that this region, which previously has been thought not to interact with lipids, also undergoes a transition into an NMR-unobservable state. It is important to note, however, that neither the 3D transferred NOE spectrum nor the methyl-to-amide NOE difference spectrum (Fig. 7) shows any evidence for NOEs beyond what is expected in a dynamically disordered random coil for this group of C-terminal residues. Similarly, no NOEs were observed between the amides of these residues and lipids (Fig. 5), even in the presence of lipid concentrations much higher than those used for Figs. 5–7 where attenuation of these amide signals is substantial (Fig. 2b). Interestingly, "break points" in the attenuation profile of the C-terminal residues (Fig. 2) coincide closely with the presence of proline residues (at positions 108, 117, 120, 128, and 138). Knowing that cis–trans isomerization of X-Pro peptide bonds, even in unstructured polypeptide chains, is slow at the temperatures used in our study (10–20 °C), and that formation of *cis* X-Pro bonds is favored in nonpolar environments,[84,85] we speculate that attenuation of the NMR signals for the 40 C-terminal residues of αS is caused by a shift in equilibrium to the cis conformation for a fraction of the X-Pro peptide bonds in this C-terminal region. The increased lipid affinity of these cis-containing protein fractions causes their signals to be invisible in the presence of lipids, yielding the observed attenuation of the remaining all-trans peptide bond protein signals. The slow kinetics of the cis–trans peptide bond equilibrium therefore could be a major factor in preventing us from studying the conformation of this region of the protein in the lipid-bound state.

If αS were to be bound to the surface of SUVs with its 100 N-terminal residues in a contiguous α-helical conformation, as concluded from recent EPR measurements,[59,60] it would occupy a minimum of 1400 Å^2—an interface that corresponds approximately to the surface area of 28 phospholipid headgroups. With two leaflets per bilayer, the minimal stoichiometry for such a binding mode therefore requires at least 56 lipids per αS molecule, assuming the surface of an SUV to be 100% covered by αS. Our present study, which shows evidence for stable lipid/αS interactions down to a 2:1 stoichiometry, clearly requires an alternative lipid-binding mode. On a more qualitative note, the slow-exchange kinetics between free αS and bound αS also appears inconsistent with such a "helix-on-a-surface" binding mode, as one would expect fraying at the ends of the helices, where there would be rapid exchange between bound state and free state, and concomitant chemical shift changes and line broadening relative to the free state.

EPR studies have provided clear evidence for the helical conformation of αS in its lipid-bound state.[59,60,86] The accessibility of this helical state to paramagnetic O_2 and chelated Ni has unambiguously shown that the hydrophobic side of the αS helix is shielded from the solvent, with the hydrophilic side being solvent-accessible.[60] We note, however, that binding modes other than a helix embedded on an SUV surface are also compatible with these EPR data. For example, a bundle of αS helices with a modest

number of phospholipids at its core could equally agree with these observations. Indeed, our TEM and cryo-EM images of lipid vesicles in the absence and in the presence of αS demonstrate that the SUVs are grossly rearranged by αS, with the presence of numerous rod-like structures, many of which appear to emerge from the vesicles (Fig. 8). Such rearrangements are consistent with earlier reports indicating that even very low concentrations of αS can result in membrane disruption and permeability, as well as vesicle leakage.[23,38,39,87]

The composition of the SUVs used in our studies has been selected to mimic that of synaptic vesicles. In purified fractions of synaptic vesicles, PS accounts for 12% of the total phospholipid content,[63] but an asymmetric distribution of PS, due to the activity of aminophospholipid translocase, nearly doubles the local concentration of PS on the cytosolic surface of the vesicle. In our studies, we observe no discontinuity in the data recorded for samples with lipid/αS ratios ranging from <1 to 150, but rather see a smooth progression in NMR spectra and other biophysical characteristics from free and disordered αS to a completely sequestered form of the protein. We do not, for example, observe the onset of fast-exchange dynamics as we would expect if αS were to be surface-bound when the protein/lipid ratio is raised. This strongly suggests the presence of relatively stable, oligomeric, lipid-bound species of αS, separated by a high-energy barrier from free and highly unstructured αS. While the majority of experiments carried out in this study were conducted under dilute lipid conditions in order to optimize the quality of the NMR spectra, titration to increasingly higher lipid concentrations shows no discontinuities, and a qualitatively similar behavior is observed over the entire range of lipid/αS ratios (Fig. 2); it is therefore likely that these conditions mimic well the physiological interactions of αS with synaptic vesicles. Our data also suggest that, in a nondiseased presynaptic environment, the population of free αS is very low, with virtually all αS molecules bound to lipids—the majority through their 100 N-terminal residues, but with a substantial fraction additionally engaging lipids through their 40 C-terminal residues. The latter mode of binding is likely to be modulated by the cis–trans equilibria of the peptide bonds preceding the five proline residues located in this region and provides a possible explanation for the recently observed presence of the cis–trans isomerase protein Pin1 in Lewy bodies.[88]

A behavior very similar to that seen here for the SUVs designed to mimic synaptic vesicles has been observed for a variety of compositions of phospholipid vesicles, with αS–membrane affinity being enhanced by negatively charged phospholipids. Fluorescence correlation spectroscopy results point to an αS affinity for 1-palmitoyl-2-oleoyl-*sn*-glycero-3-phospho-L-serine[53] that is comparable to the K_d of 50 μM estimated from our study.

The presence of a set of stable but distinctly different binding modes, which engage different lengths of the αS sequence, differentiates our results from those of earlier studies. It is interesting to speculate how the presence of these stable binding modes may relate to αS fibril formation, often considered the hallmark of Parkinson's disease. Biophysical characterization has implicated the so-called NAC region of the protein (residues 65–95) to engage in extended β-sheets that make up the fibrils.[28,29] Clearly, such fibril formation is not directly possible for the SL2 binding mode, where all 100 N-terminal residues are in a helical state, but it would be readily possible for SL1, where only the 25 N-terminal residues are found to be sequestered in a helical state. In fact, one would expect the SL1 binding mode to promote fibril formation, as anchoring of the N-terminal region of many αS proteins in the "dark-state" particle leaves a very high local concentration of dynamically disordered fibril-formation-prone NAC regions on its surface.[27] These results also explain the previous paradox, where the presence of low concentrations of phospholipids was found to promote fibril formation,[37–42] as they would correspond to elevated SL1 binding modes whereas high phospholipid concentrations were found to protect against fibril formation.[37–42] The latter result is also expected on the basis of our results, as high phospholipid concentrations promote not only the SL2 binding mode but also binding modes that are likely to protect the C-terminus, protecting the NAC region from forming β-sheets. Prior explanations for the increased fibril formation at low-lipid or low-detergent concentrations simply focused on the increased local concentration of αS;[27,40] our results suggest that the anchoring of the α-helical N-terminal domains of αS molecules not only results in an increased local concentration of unstructured NAC domains but also causes them to be lined up in a roughly parallel arrangement, thereby promoting the formation of parallel β-sheet fibril structures.

The disease-associated αS gene-triplicating mutant[89] increases the αS concentration *in vivo* and thereby promotes the SL1 binding mode, elevating the concentration of fibril-formation-prone NAC regions by much more than just the effect of the increased cellular concentration. Similarly, it is likely that the disease-causing A30P mutant,[4] which is helix-disrupting, will shift the equilibrium of binding modes towards SL1 because the helical conformation of residue 30 in the native binding modes (i.e., SL2) is energetically unfavorable. In this respect, it is interesting to note that A30P mutation increases, relative to wild type, the population of free αS in an NMR study employing POPA/POPC vesicles.[13] NMR studies of the lipid-binding properties of this mutant, as well as those of the other disease-causing mutants E46K and A53T, are currently in progress.

Materials and Methods

Expression and purification of αS protein

Human wild-type αS cloned in the kanamycin-restricted pET41a vector was overexpressed in *Escherichia*

coli. For NMR samples, ^{15}N–^{2}H isotopic enrichment of the protein was achieved by culturing cells in M9 minimal media: 6 g L^{-1} $Na_2HPO_4{\cdot}7H_2O$, 3 g L^{-1} KH_2PO_4, 5 g L^{-1} NaCl, 1 mM $MgSO_4$, 100 μM $CaCl_2$, 3.0 g L^{-1} perdeuterated D-glucose, 1 g L^{-1} $^{15}NH_4Cl$, and 1 g L^{-1} ^{15}N,^{2}H-rich growth medium supplement (Celtone; Cambridge Isotope Laboratories, Andover, MA) in D_2O. For proteins with specific $^{13}C^{1}H_3$ labeling of valine, leucine, and isoleucine side chains, *E. coli* was grown without a rich growth medium supplement, and the precursors [$3^{2}H$]α-ketoisovalerate (100 mg L^{-1}) and [3,$3^{2}H_2$]α-ketobutyrate (50 mg L^{-1}) were added an hour prior to induction, in accordance with the protocol of Goto *et al.*[79] Protein expression was induced with 1 mM IPTG at $A_{600}=0.6$–0.8 for 4.5 h. Lysis of the cells and purification of the protein were achieved by freeze–thaw cycles, followed by heat precipitation (15 min, 80 °C) in 50 mM Tris–HCl (pH 7.4) and 500 mM NaCl. Anion-exchange chromatography on a Q-Sepharose column (Amersham Biosciences, Piscataway, NJ) was employed as a final purification step and yielded αS with >98% purity, as analyzed by SDS-PAGE. The purified protein was dialyzed into water and lyophilized for storage.

Preparation of SUVs

Phospholipids were purchased as a lyophilized mixture (5:3:2 DOPE/DOPS/DOPC) from Avanti Polar Lipids (Alabaster, AL) and used without further purification. The lipid mixture was weighed out, and 20 mM Na_2HPO_4 (pH 7.0) added to achieve a 15% (wt/vol) opaque, viscous slurry. The mixture was alternately subjected to vortex mixing and probe sonication to achieve vesicles of small diameter (20–40 nm, as determined by DLS; data not shown). After sonication, the vesicle solution turned hazy blue and was much less viscous than the starting suspension. More dilute solutions of SUVs were made, as necessary, for experimental purposes, but were always diluted from a stock solution prepared as described above at 15% (wt/vol).

NMR spectroscopy

NMR spectra were recorded at 293 K on Bruker spectrometers operating at ^{1}H frequencies of 600, 750, and 800 MHz and equipped with cryogenic (600 and 800 MHz) or room-temperature (750 MHz) probes. Data were processed using NMRPipe software[90] and analyzed by NMRPipe and Sparky software (Goddard T. D. & Kneller D. G., unpublished data). Samples were prepared from lyophilized protein dissolved in 20 mM Na_2HPO_4 (pH 6.0), 94%/6% H_2O/D_2O, and 0.02% NaN_3, and concentrations were determined by UV–Vis spectra using an extinction coefficient of $\varepsilon_{280}=5120\ M^{-1}\ cm^{-1}$.

For experiments in which lipids were titrated into the sample, HSQC spectra were recorded with a data matrix consisting of 1280 (t_2, ^{1}H)×448 (t_1, ^{15}N) complex points, $t_{2,max}=152$ ms, and $t_{1,max}=334$ ms. Lipid-to-amide resonance NOE transfer experiments were recorded in difference mode as two interleaved HSQC experiments, applying a 1.5-s presaturation pulse with a radiofrequency field strength of 21 Hz centered at either 1.16 or −10 ppm. The ^{15}N TROSY experiments for R_2^{T} measurement[66,91] were recorded as interleaved experiments with 12 T_2 delays (20, 30, 50, 70, 90, 120, 150, 180, 220, 270, 400, and 500 ms) and acquisition times matching those of regular HSQC experiments. The 3D HMQC-NOE-HMQC spectrum was recorded with a mixing time of 100 ms and a ^{1}H frequency of 600 MHz as a data matrix consisting of 2048 (t_3, ^{1}H)×84 (t_2, ^{15}N)×84 (t_1, ^{15}N) complex points, $t_{3,max}=106$ ms, $t_{2,max}=60.8$ ms, and $t_{1,max}=60.8$ ms. The complementary 3D NOESY-HMQC spectrum was recorded with the same mixing time and 2048 (t_3, ^{1}H)×84 (t_2, ^{15}N)×72 (t_1, ^{1}H) complex points, $t_{3,max}=106$ ms, $t_{2,max}=60.8$ ms, and $t_{1,max}=48$ ms. Amide-selective EBURP and REBURP pulses,[77] of 1.8 ms duration each and centered at 8.3 ppm, were used for both experiments.

Leu-$C^{\delta1}H_3$ inversion experiments were measured by interleaving ^{1}H–^{15}N HSQC experiments where, in alternate scans, $C^{\delta1}H_3$ proton resonance is inverted by means of a bilinear pulse, taking advantage of the fact that Leu-$^{13}C^{\delta1}$ resonates more than 5 ppm downfield from the other methyl groups of valine and isoleucine. A bilinear pulse[80,81] of the type $90_x(^{1}H)$-τ-[$180_x(^{1}H)/180_x(^{13}C^{\delta1})_{on/off}$]-τ-$90_x(^{1}H)$—where the pulses in square brackets are centered relative to one another, $180_x(^{13}C^{\delta1})$ is a 7-ms REBURP-shaped pulse, and τ=1.2 ms—was used for selective inversion. The NOE mixing time between the bilinear pulse and the HSQC experiment was 250 ms.

PFG NMR experiments for determining the self-diffusion rates of protein and lipid were carried out at a ^{1}H frequency of 600 MHz, using a room-temperature, three-axis-gradient, triple-resonance probehead. Experiments were recorded as one-dimensional spectra readout after variable-strength, two-axis (*yz*)-gradient encoding and decoding[92] separated by a 500-ms diffusion delay. The reference intensity spectrum was taken at 6% of the maximum gradient strength (87 G cm^{-1}). All spectra were recorded at 10 °C.

Electron microscopy

For cryo-EM imaging, vitrified samples were prepared in a Vitrobot apparatus (FEI Company, Hillsboro, OR) at a relative humidity of 85%. A 5-μL sample volume of 0.03% DOPE/DOPS/DOPC SUV either in the absence or in the presence of 600 μM αS was applied to a plasma holey-carbon-coated grid (Quantifoil, Hatfield, PA) and blotted with filter paper for 1 s to leave a thin film of solution. Blotted samples were immediately plunged into liquid ethane at its freezing point (−196 °C) and stored under liquid nitrogen prior to imaging under a microscope. Samples were examined using a Philips CM120 electron microscope operating at 100 kV, using a Gatan 626 cryo-holder cooled with liquid nitrogen to temperatures below −180 °C. Digital images were acquired on a Gatan 791 MultiScan CCD camera with the DigitalMicrograph software package (Gatan, Pleasanton, CA).

Fluorescence anisotropy

Fluorescence anisotropy measurements were taken on a Jobin Yvon Fluoromax3 fluorimeter with automatic polarizers. Data were recorded at 25 °C with an excitation wavelength of 280 nm, a bandwidth of 2 nm, and an integration of 3 s. Emission values were recorded at 306 nm, the emission maximum for tyrosine. Each data point is the average of 10 measurements.

Acknowledgements

This work was funded by the Intramural Research Program of the National Institute of Diabetes and

Digestive and Kidney Diseases, National Institutes of Health (to A.B.), and by the Leverhulme Trust and the Wellcome Trust (to C.M.D.). We thank James Masse, Nick Fitzkee, Frank Delaglio, and Alex Grishaev for help with data analysis; Jenny Hinshaw (National Institute of Diabetes and Digestive and Kidney Diseases), Dan Shi, and Sriram Subramanian (National Cancer Institute) for help with cryo-EM data collection and interpretation; and John Christodolou for valuable help in the initial phase of this study.

Supplementary Data

Supplementary data associated with this article can be found, in the online version, at doi:10.1016/j.jmb.2009.05.066

References

1. Spillantini, M. G., Crowther, R. A., Jakes, R., Hasegawa, M. & Goedert, M. (1998). Alpha-synuclein in filamentous inclusions of Lewy bodies from Parkinson's disease and dementia with Lewy bodies. *Proc. Natl Acad. Sci. USA*, **95**, 6469–6473.
2. Spillantini, M. G., Schmidt, M. L., Lee, V. M. Y., Trojanowski, J. Q., Jakes, R. & Goedert, M. (1997). Alpha-synuclein in Lewy bodies. *Nature*, **388**, 839–840.
3. Polymeropoulos, M. H., Lavedan, C., Leroy, E., Ide, S. E., Dehejia, A., Dutra, A. *et al.* (1997). Mutation in the alpha-synuclein gene identified in families with Parkinson's disease. *Science*, **276**, 2045–2047.
4. Kruger, R., Kuhn, W., Muller, T., Woitalla, D., Graeber, M., Kosel, S. *et al.* (1998). Ala30Pro mutation in the gene encoding alpha-synuclein in Parkinson's disease. *Nat. Genet.* **18**, 106–108.
5. Zarranz, J. J., Alegre, J., Gomez-Esteban, J. C., Lezcano, E., Ros, R., Ampuero, I. *et al.* (2004). The new mutation, E46K, of alpha-synuclein causes Parkinson and Lewy body dementia. *Ann. Neurol.* **55**, 164–173.
6. Iwai, A., Masliah, E., Yoshimoto, M., Ge, N. F., Flanagan, L., Desilva, H. A. R. *et al.* (1995). The precursor protein of non-A-beta component of Alzheimer's-disease amyloid is a presynaptic protein of the central nervous system. *Neuron*, **14**, 467–475.
7. Weinreb, P. H., Zhen, W. G., Poon, A. W., Conway, K. A. & Lansbury, P. T. (1996). NACP, a protein implicated in Alzheimer's disease and learning, is natively unfolded. *Biochemistry*, **35**, 13709–13715.
8. Maroteaux, L., Campanelli, J. T. & Scheller, R. H. (1988). Synuclein—a neuron-specific protein localized to the nucleus and presynaptic nerve terminal. *J. Neurosci.* **8**, 2804–2815.
9. Withers, G. S., George, J. M., Banker, G. A. & Clayton, D. F. (1997). Delayed localization of synelfin (synuclein, NACP) to presynaptic terminals in cultured rat hippocampal neurons. *Dev. Brain Res.* **99**, 87–94.
10. Kahle, P. J., Neumann, M., Ozmen, L., Muller, V., Jacobsen, H., Schindzielorz, A. *et al.* (2000). Subcellular localization of wild-type and Parkinson's disease-associated mutant alpha-synuclein in human and transgenic mouse brain. *J. Neurosci.* **20**, 6365–6373.
11. Jensen, P. H., Nielsen, M. S., Jakes, R., Dotti, G. & Goedert, M. (1998). Binding of alpha-synuclein to brain vesicles is abolished by familial Parkinson's disease mutation. *J. Biol. Chem.* **273**, 26292–26294.
12. Irizarry, M. C., Kim, T. W., McNamara, M., Tanzi, R. E., George, J. M., Clayton, D. F. & Hyman, B. T. (1996). Characterization of the precursor protein of the non-A beta component of senile plaques (NACP) in the human central nervous system. *J. Neuropathol. Exp. Neurol.* **55**, 889–895.
13. Bussell, R. & Eliezer, D. (2004). Effects of Parkinson's disease-linked mutations on the structure of lipid-associated alpha-synuclein. *Biochemistry*, **43**, 4810–4818.
14. Abeliovich, A., Schmitz, Y., Farinas, I., Choi-Lundberg, D., Ho, W. H., Castillo, P. E. *et al.* (2000). Mice lacking alpha-synuclein display functional deficits in the nigrostriatal dopamine system. *Neuron*, **25**, 239–252.
15. Murphy, D. D., Rueter, S. M., Trojanowski, J. Q. & Lee, V. M. Y. (2000). Synucleins are developmentally expressed, and alpha-synuclein regulates the size of the presynaptic vesicular pool in primary hippocampal neurons. *J. Neurosci.* **20**, 3214–3220.
16. Cabin, D. E., Shimazu, K., Murphy, D., Cole, N. B., Gottschalk, W., McIlwain, K. L. *et al.* (2002). Synaptic vesicle depletion correlates with attenuated synaptic responses to prolonged repetitive stimulation in mice lacking alpha-synuclein. *J. Neurosci.* **22**, 8797–8807.
17. Schluter, O. M., Fornai, F., Alessandri, M. G., Takamori, S., Geppert, M., Jahn, R. & Sudhof, T. C. (2003). Role of alpha-synuclein in 1-methyl-4-phenyl-1,2,3,6-tetra-hydropyridine-induced parkinsonism in mice. *Neuroscience*, **118**, 985–1002.
18. Nuscher, B., Kamp, F., Mehnert, T., Odoy, S., Haass, C., Kahle, P. J. & Beyer, K. (2004). Alpha-synuclein has a high affinity for packing defects in a bilayer membrane—a thermodynamics study. *J. Biol. Chem.* **279**, 21966–21975.
19. Lee, F. J. S., Liu, F., Pristupa, Z. B. & Niznik, H. B. (2001). Direct binding and functional coupling of alpha-synuclein to the dopamine transporters accelerate dopamine-induced apoptosis. *FASEB J.* **15**, 916–926.
20. Perez, R. G., Waymire, J. C., Lin, E., Liu, J. J., Guo, F. L. & Zigmond, M. J. (2002). A role for alpha-synuclein in the regulation of dopamine biosynthesis. *J. Neurosci.* **22**, 3090–3099.
21. Lotharius, J. & Brundin, P. (2002). Impaired dopamine storage resulting from alpha-synuclein mutations may contribute to the pathogenesis of Parkinson's disease. *Hum. Mol. Genet.* **11**, 2395–2407.
22. Davidson, W. S., Jonas, A., Clayton, D. F. & George, J. M. (1998). Stabilization of alpha-synuclein secondary structure upon binding to synthetic membranes. *J. Biol. Chem.* **273**, 9443–9449.
23. Jo, E. J., McLaurin, J., Yip, C. M., St George-Hyslop, P. & Fraser, P. E. (2000). Alpha-synuclein membrane interactions and lipid specificity. *J. Biol. Chem.* **275**, 34328–34334.
24. McLean, P. J., Kawamata, H., Ribich, S. & Hyman, B. T. (2000). Membrane association and protein conformation of alpha-synuclein in intact neurons—effect of Parkinson's disease-linked mutations. *J. Biol. Chem.* **275**, 8812–8816.
25. Perrin, R. J., Woods, W. S., Clayton, D. F. & George, J. M. (2000). Interaction of human alpha-synuclein and Parkinson's disease variants with phospholipids—structural analysis using site-directed mutagenesis. *J. Biol. Chem.* **275**, 34393–34398.
26. Chandra, S., Chen, X. C., Rizo, J., Jahn, R. & Sudhof, T. C. (2003). A broken alpha-helix in folded alpha-synuclein. *J. Biol. Chem.* **278**, 15313–15318.

27. Rivers, R. C., Kumita, J. R., Tartaglia, G. G., Dedmon, M. M., Pawar, A., Vendruscolo, M. *et al.* (2008). Molecular determinants of the aggregation behavior of alpha- and beta-synuclein. *Protein Sci.* **17**, 887–898.
28. Bodles, A. M., Guthrie, D. J. S., Greer, B. & Irvine, G. B. (2001). Identification of the region of non-A beta component (NAC) of Alzheimer's disease amyloid responsible for its aggregation and toxicity. *J. Neurochem.* **78**, 384–395.
29. Giasson, B. I., Murray, I. V. J., Trojanowski, J. Q. & Lee, V. M. Y. (2001). A hydrophobic stretch of 12 amino acid residues in the middle of alpha-synuclein is essential for filament assembly. *J. Biol. Chem.* **276**, 2380–2386.
30. Dedmon, M. M., Lindorff-Larsen, K., Christodoulou, J., Vendruscolo, M. & Dobson, C. M. (2005). Mapping long-range interactions in alpha-synuclein using spin-label NMR and ensemble molecular dynamics simulations. *J. Am. Chem. Soc.* **127**, 476–477.
31. Bertoncini, C. W., Jung, Y. S., Fernandez, C. O., Hoyer, W., Griesinger, C., Jovin, T. M. & Zweckstetter, M. (2005). Release of long-range tertiary interactions potentiates aggregation of natively unstructured alpha-synuclein. *Proc. Natl Acad. Sci. USA*, **102**, 1430–1435.
32. Bussell, R. & Eliezer, D. (2001). Residual structure and dynamics in Parkinson's disease-associated mutants of alpha-synuclein. *J. Biol. Chem.* **276**, 45996–46003.
33. Eliezer, D., Kutluay, E., Bussell, R. & Browne, G. (2001). Conformational properties of alpha-synuclein in its free and lipid-associated states. *J. Mol. Biol.* **307**, 1061–1073.
34. Bussell, R. & Eliezer, D. (2003). A structural and functional role for 11-mer repeats in alpha-synuclein and other exchangeable lipid binding proteins. *J. Mol. Biol.* **329**, 763–778.
35. Ulmer, T. S. & Bax, A. (2005). Comparison of structure and dynamics of micelle-bound human alpha-synuclein and Parkinson disease variants. *J. Biol. Chem.* **280**, 43179–43187.
36. Ulmer, T. S., Bax, A., Cole, N. B. & Nussbaum, R. L. (2005). Structure and dynamics of micelle-bound human alpha-synuclein. *J. Biol. Chem.* **280**, 9595–9603.
37. Perrin, R. J., Woods, W. S., Clayton, D. F. & George, J. M. (2001). Exposure to long chain polyunsaturated fatty acids triggers rapid multimerization of synucleins. *J. Biol. Chem.* **276**, 41958–41962.
38. Zhu, M. & Fink, A. L. (2003). Lipid binding inhibits alpha-synuclein fibril formation. *J. Biol. Chem.* **278**, 16873–16877.
39. Zhu, M., Li, J. & Fink, A. L. (2003). The association of alpha-synuclein with membranes affects bilayer structure, stability, and fibril formation. *J. Biol. Chem.* **278**, 40186–40197.
40. Necula, M., Chirita, C. N. & Kuret, J. (2003). Rapid anionic micelle-mediated alpha-synuclein fibrillization *in vitro*. *J. Biol. Chem.* **278**, 46674–46680.
41. Welch, K. & Yuan, J. Y. (2003). Alpha-synuclein oligomerization: a role for lipids? *Trends Neurosci.* **26**, 517–519.
42. Jo, E., Darabie, A. A., Han, K., Tandon, A., Fraser, P. E. & McLaurin, J. (2004). Alpha-synuclein–synaptosomal membrane interactions—implications for fibrillogenesis. *Eur. J. Biochem.* **271**, 3180–3189.
43. Volles, M. J., Lee, S. J., Rochet, J. C., Shtilerman, M. D., Ding, T. T., Kessler, J. C. & Lansbury, P. T. (2001). Vesicle permeabilization by protofibrillar alpha-synuclein: implications for the pathogenesis and treatment of Parkinson's disease. *Biochemistry*, **40**, 7812–7819.
44. Volles, M. J. & Lansbury, P. T. (2002). Vesicle permeabilization by protofibrillar alpha-synuclein is sensitive to Parkinson's disease-linked mutations and occurs by a pore-like mechanism. *Biochemistry*, **41**, 4595–4602.
45. Lashuel, H. A., Petre, B. M., Wall, J., Simon, M., Nowak, R. J., Walz, T. & Lansbury, P. T. (2002). Alpha-synuclein, especially the Parkinson's disease-associated mutants, forms pore-like annular and tubular protofibrils. *J. Mol. Biol.* **322**, 1089–1102.
46. Ding, T. T., Lee, S. J., Rochet, J. C. & Lansbury, P. T. (2002). Annular alpha-synuclein protofibrils are produced when spherical protofibrils are incubated in solution or bound to brain-derived membranes. *Biochemistry*, **41**, 10209–10217.
47. Quist, A., Doudevski, L., Lin, H., Azimova, R., Ng, D., Frangione, B. *et al.* (2005). Amyloid ion channels: a common structural link for protein-misfolding disease. *Proc. Natl Acad. Sci. USA*, **102**, 10427–10432.
48. Zakharov, S. D., Hulleman, J. D., Dutseva, E. A., Antonenko, Y. N., Rochet, J. C. & Cramer, W. A. (2007). Helical alpha-synuclein forms highly conductive ion channels. *Biochemistry*, **46**, 14369–14379.
49. Adamczyk, A. & Strosznajder, J. B. (2006). Alpha-synuclein potentiates Ca^{2+} influx through voltage-dependent Ca^{2+} channels. *NeuroReport*, **17**, 1883–1886.
50. Beyer, K. (2007). Mechanistic aspects of Parkinson's disease: alpha-synuclein and the biomembrane. *Cell Biochem. Biophys.* **47**, 285–299.
51. Ramakrishnan, M., Jensen, P. H. & Marsh, D. (2003). Alpha-synuclein association with phosphatidylglycerol probed by lipid spin labels. *Biochemistry*, **42**, 12919–12926.
52. Narayanan, V. & Scarlata, S. (2001). Membrane binding and self-association of alpha-synucleins. *Biochemistry*, **40**, 9927–9934.
53. Rhoades, E., Ramlall, T. F., Webb, W. W. & Eliezer, D. (2006). Quantification of alpha-synuclein binding to lipid vesicles using fluorescence correlation spectroscopy. *Biophys. J.* **90**, 4692–4700.
54. Kubo, S., Nemani, V. M., Chalkley, R. J., Anthony, M. D., Hattori, N., Mizuno, Y. *et al.* (2005). A combinatorial code for the interaction of alpha-synuclein with membranes. *J. Biol. Chem.* **280**, 31664–31672.
55. Kamp, F. & Beyer, K. (2006). Binding of alpha-synuclein affects the lipid packing in bilayers of small vesicles. *J. Biol. Chem.* **281**, 9251–9259.
56. Stockl, M., Fischer, P., Wanker, E. & Herrmann, A. (2008). Alpha-synuclein selectively binds to anionic phospholipids embedded in liquid-disordered domains. *J. Mol. Biol.* **375**, 1394–1404.
57. Fortin, D. L., Troyer, M. D., Nakamura, K., Kubo, S., Anthony, M. D. & Edwards, R. H. (2004). Lipid rafts mediate the synaptic localization of alpha-synuclein. *J. Neurosci.* **24**, 6715–6723.
58. Kubo, S., Fortin, D. L., Nemani, V. M., Hattori, N., Mizuno, Y. & Edwards, R. H. (2006). Alpha-synuclein associates with lipid rafts *in vitro*. *Mov. Disord.* **21**, S351–S352.
59. Georgieva, E. R., Ramlall, T. F., Borbat, P. P., Freed, J. H. & Eliezer, D. (2008). Membrane-bound alpha-synuclein forms an extended helix: long-distance pulsed ESR measurements using vesicles, bicelles, and rodlike micelles. *J. Am. Chem. Soc.* **130**, 12856–12857.
60. Jao, C. C., Hegde, B. G., Chen, J., Haworth, I. S. & Langen, R. (2008). Structure of membrane-bound α-synuclein from site-directed spin labeling and computational refinement. *Proc. Natl Acad. Sci. USA*, **105**, 19666–19771.

61. Drescher, M., Godschalk, F., Veldhuis, G., van Rooijen, B. D., Subramaniam, V. & Huber, M. (2008). Spin-label EPR on alpha-synuclein reveals differences in the membrane binding affinity of the two antiparallel helices. *ChemBioChem*, **9**, 2411–2416.
62. Bortolus, M., Tombolato, F., Tessari, I., Bisaglia, M., Mammi, S., Bubacco, L. *et al.* (2008). Broken helix in vesicle and micelle-bound alpha-synuclein: insights from site-directed spin labeling—EPR experiments and MD simulations. *J. Am. Chem. Soc.* **130**, 6690–6691.
63. Takamori, S., Holt, M., Stenius, K., Lemke, E. A., Gronborg, M., Riedel, D. *et al.* (2006). Molecular anatomy of a trafficking organelle. *Cell*, **127**, 831–846.
64. Lipari, G. & Szabo, A. (1982). Model-free approach to the interpretation of nuclear magnetic resonance relaxation in macromolecules: 1. Theory and range of validity. *J. Am. Chem. Soc.* **104**, 4546–4559.
65. Pervushin, K., Riek, R., Wider, G. & Wuthrich, K. (1997). Attenuated *T*-2 relaxation by mutual cancellation of dipole–dipole coupling and chemical shift anisotropy indicates an avenue to NMR structures of very large biological macromolecules in solution. *Proc. Natl Acad. Sci. USA*, **94**, 12366–12371.
66. Igumenova, T. I. & Palmer, A. G. (2006). Off-resonance TROSY-selected R-1p experiment with improved sensitivity for medium- and high-molecular-weight proteins. *J. Am. Chem. Soc.* **128**, 8110–8111.
67. Wang, C. Y., Rance, M. & Palmer, A. G. (2003). Mapping chemical exchange in proteins with MW>50 kD. *J. Am. Chem. Soc.* **125**, 8968–8969.
68. Bai, Y., Milne, J. S. & Englander, S. W. (1993). Primary structure effects on peptide group exchange. *Proteins*, **17**, 75–86.
69. Bernado, P., Bertoncini, C. W., Griesinger, C., Zweckstetter, M. & Blackledge, M. (2005). Defining long-range order and local disorder in native alpha-synuclein using residual dipolar couplings. *J. Am. Chem. Soc.* **127**, 17968–17969.
70. Sung, Y. H. & Eliezer, D. (2007). Residual structure, backbone dynamics, and interactions within the synuclein family. *J. Mol. Biol.* **372**, 689–707.
71. Siemer, A. B., Arnold, A. A., Ritter, C., Westfeld, T., Ernst, M., Riek, R. & Meier, B. H. (2006). Observation of highly flexible residues in amyloid fibrils of the HET-s prion. *J. Am. Chem. Soc.* **128**, 13224–13228.
72. Clore, G. M. & Gronenborn, A. M. (1983). Theory of the time dependent transferred nuclear Overhauser effect: applications to structural analysis of ligand–protein complexes in solution. *J. Magn. Reson.* **53**, 423–442.
73. Ni, F. (1994). Recent developments in transferred NOE methods. *Prog. NMR Spectrosc.* **26**, 517–606.
74. Frenkiel, T., Bauer, C., Carr, M. D., Birdsall, B. & Feeney, J. (1990). HMQC-NOESY-HMQC, a 3-dimensional NMR experiment which allows detection of nuclear Overhauser effects between protons with overlapping signals. *J. Magn. Reson.* **90**, 420–425.
75. Ikura, M., Bax, A., Clore, G. M. & Gronenborn, A. M. (1990). Detection of nuclear Overhauser effects between degenerate amide proton resonances by heteronuclear three-dimensional nuclear magnetic resonance spectroscopy. *J. Am. Chem. Soc.* **112**, 9020–9022.
76. Ikura, M., Kay, L. E., Tschudin, R. & Bax, A. (1990). Three-dimensional NOESY-HMQC spectroscopy of a ^{13}C-labeled protein. *J. Magn. Reson.* **86**, 204–209.
77. Geen, H. & Freeman, R. (1991). Band-selective radiofrequency pulses. *J. Magn. Reson.* **93**, 93–141.
78. Schanda, P. & Brutscher, B. (2005). Very fast two-dimensional NMR spectroscopy for real-time investigation of dynamic events in proteins on the time scale of seconds. *J. Am. Chem. Soc.* **127**, 8014–8015.
79. Goto, N. K., Gardner, K. H., Mueller, G. A., Willis, R. C. & Kay, L. E. (1999). A robust and cost-effective method for the production of Val, Leu, Ile (delta 1) methyl-protonated N-15-, C-13-, H-2-labeled proteins. *J. Biomol. NMR*, **13**, 369–374.
80. Garbow, J. R., Weitekamp, D. P. & Pines, A. (1982). Bilinear rotation decoupling of homonuclear scalar interactions. *Chem. Phys. Lett.* **93**, 504–509.
81. Bax, A. (1983). Broad-band homonuclear decoupling in heteronuclear shift correlation NMR spectroscopy. *J. Magn. Reson.* **53**, 517–520.
82. Price, W. S. (1997). Pulsed-field gradient nuclear magnetic resonance as a tool for studying translational diffusion: 1. Basic theory. *Concepts Magn. Reson.* **9**, 299–336.
83. Schulman, B. A., Kim, P. S., Dobson, C. M. & Redfield, C. (1997). A residue-specific NMR view of the non-cooperative unfolding of a molten globule. *Nat. Struct. Biol.* **4**, 630–634.
84. Gao, X. F. & Wong, T. C. (2001). NMR studies of adrenocorticotropin hormone peptides in sodium dodecylsulfate and dodecylphosphocholine micelles: proline isomerism and interactions of the peptides with micelles. *Biopolymers*, **58**, 20–32.
85. Torchia, D. A. (1972). Evidence for cis peptide bonds in copolypeptides of glycine and proline. *Biochemistry*, **11**, 1462–1468.
86. Bortolus, M., Tombolato, F., Tessari, I., Bisaglia, M., Mammi, S., Bubacco, L. *et al.* (2008). Broken helix in vesicle and micelle-bound alpha-synuclein: insights from site-directed spin labeling—EPR experiments and MD simulations. *J. Am. Chem. Soc.* **130**, 6690–6691.
87. Madine, J., Hughes, E., Doig, A. J. & Middleton, D. A. (2008). The effects of α-synuclein on phospholipid vesicle integrity: a study using ^{31}P NMR and electron microscopy. *Mol. Membr. Biol.* **25**, 518–527.
88. Ryo, A., Togo, T., Nakai, T., Hirai, A., Nishi, M., Yamaguchi, A., Suzuki, K., Hirayasu, Y., Kobayashi, H., Perrem, K., Liou, Y. C. & Aoki, I. (2006). Prolyl-isomerase Pin1 accumulates in lewy bodies of parkinson disease and facilitates formation of alpha-synuclein inclusions. *J. Biol. Chem.* **281**, 4117–4125.
89. Singleton, A. B., Farrer, M., Johnson, J., Singleton, A., Hague, S., Kachergus, J. *et al.* (2003). Alpha-synuclein locus triplication causes Parkinson's disease. *Science*, **302**, 841.
90. Delaglio, F., Grzesiek, S., Vuister, G. W., Zhu, G., Pfeifer, J. & Bax, A. (1995). NMRPipe—a multidimensional spectral processing system based on Unix pipes. *J. Biomol. NMR*, **6**, 277–293.
91. Wang, C. Y., Rance, M. & Palmer, A. G. (2003). Mapping chemical exchange in proteins with MW> 50 kD. *J. Am. Chem. Soc.* **125**, 8968–8969.
92. Chou, J. J., Baber, J. L. & Bax, A. (2004). Characterization of phospholipid mixed micelles by translational diffusion. *J. Biomol. NMR*, **29**, 299–308.